HARMONI at ELT: full scale prototype of the laser guide star wavefront sensor

Pierre Jouve, Felipe Pedreros Bustos, Anne Costille, Benoit Neichel, Thierry Fusco, Kjetil Dolhen

HARMONI at ELT: Full scale prototype of the laser guide star wavefront sensor

Pierre Jouve[a,*], Felipe Pedreros Bustos[a], Anne Costille[a], Benoit Neichel[a], Thierry Fusco[b,a], and Kjetil Dohlen[a]

[a]Aix Marseille Université, CNRS, CNES, Laboratoire d'Astrophysique de Marseille, Marseille, France
[b]DOTA, ONERA, Université Paris Saclay (COmUE), Châtillon, France

ABSTRACT

HARMONI is the first light visible and near-IR integral field spectrograph for the ELT. It covers a large spectral range from 450 nm to 2450 nm with resolving powers from 3500 to 18000 and spatial sampling from 60 mas to 4 mas. It can operate in two Adaptive Optics modes - SCAO (including a High Contrast capability) and LTAO - or with no AO mode. To prepare the final design reviews, we have built an optical bench to emulate and characterize the performance of the laser guide star (LGS) wavefront sensor (WFS) to be used in HARMONI. The WFS is a classic Shack-Hartmann, nonetheless pushed to the extreme due to the size of the primary mirror of the ELT (39 m). The WFS is composed of a 80×80 double side microlens array (MLA), an optical relay made of 6 lenses in order to re-image the light coming from the MLA on the detector, and a CMOS camera using a Sony detector with 1608×1104 pixels, RON$< 3e$, and a frame rate of 500Hz. The sensor has a large number of pixels to provide a field-of-view wider than 15 arcsec per subaperture over the full pupil, which is required to image the elongated LGS spots. An innovative feature of our bench is the use of a spatial light modulator (SLM) which allows us to emulate the M4 deformable mirror (DM) and the real position of its actuators, together with the projected spiders in the pupil plane. We report on the design and performance of our bench, including the first interaction matrices using the ELT-M4 influence functions and a non-elongated source. We expect to implement a system to emulate an elongated source in order to grasp a better understanding of its effects on wavefront sensing.

*contact author: pierre.jouve@lam.fr

Keywords: WaveFront sensor, ELT, HARMONI, elongated source, SLM.

1. INTRODUCTION

HARMONI is a near-infrared integral field spectrograph, providing the European Southern Observatory (ESO) Extremely Large Telescope (ELT) core spectroscopic capability.[1] HARMONI is led by a consortium of 6 partners - two from UK: Oxford University (PI institute), UK-ATC; two from Spain: IAC in Tenerife, and the CAB in Madrid; and two from France: CRAL in Lyon and LAM in Marseille. On top of that, four associate partners are also working with the HARMONI team; these are the University of Durham, ONERA (Paris), IPAG (Grenoble) and RAL Space.

HARMONI will be able to operate at diffraction limited scales thanks to two adaptive optics systems complementary to each other: a Single Conjugate Adaptive Optics (SCAO) system for good performance and narrow field of view, and a Laser Tomographic AO (LTAO) system for medium performance and very good sky coverage.[2]

The prototype described in this paper is directly related to the Laser guide star sensor[3] (LGSS) that will be integrated in the LAM.

This bench will enable to verify the LGS WFS design and to explore experimentally new concepts of LGS wavefront sensing at the ELT scale, such as super-resolution[4] .

1.1 Specifications

The projection angle of an elongated laser guide star at a given point over the telescope pupil can be well approximated with the following equation:

$$\theta_{\text{elongation}} = \frac{L_{\text{base}} \Delta h \sec(\zeta)}{[H \sec(\zeta)]^2 + [H \Delta h \sec(\zeta)]^2}, \tag{1}$$

where L_{base} is the horizontal separation between the laser launch telescope and the point of observation, H is the vertical distance between the telescope and the base of the sodium layer, Δh is the vertical thickness of the sodium layer, and ζ is the zenith angle.

Studies show that the minimum vertical altitude of the sodium layer centroid is as low as 84.8 km, while the maximum centroid altitude reaches 95 km (above sea level). The width is better described in term of the seven "typical profiles" whose width range from 13 km up to 20 km.[5] For median conditions, $H = 80$ km (above the ELT site, 3060 m a.s.l.), $\Delta h = 19$ km, and $\zeta = 30°$ and for a point opposite to the laser launch telescope on the ELT pupil $L_{\text{base}} = 39$ m, the LGS elongation perspective angle is $\theta_{\text{elongation}} = 16.7$ arcsec.

The non-elongated or short axis of the LGS depends of the laser beam size, seeing conditions and propagation distance. A formula to determine the full-width-half-maximum (FWHM) of the LGS spot at the Very Large Telescope (VLT) is presented by Holzlöhner et al.,[6] as a function of seeing, diameter of the laser launch telescope and wavefront error. Figure 1 shows the size of the LGS in the elongated and non-elongated directions. The short axis is shown at three seeing conditions, where 0.66 arcsec is the median seeing in Paranal, assuming a launch telescope of 30 cm diameter.

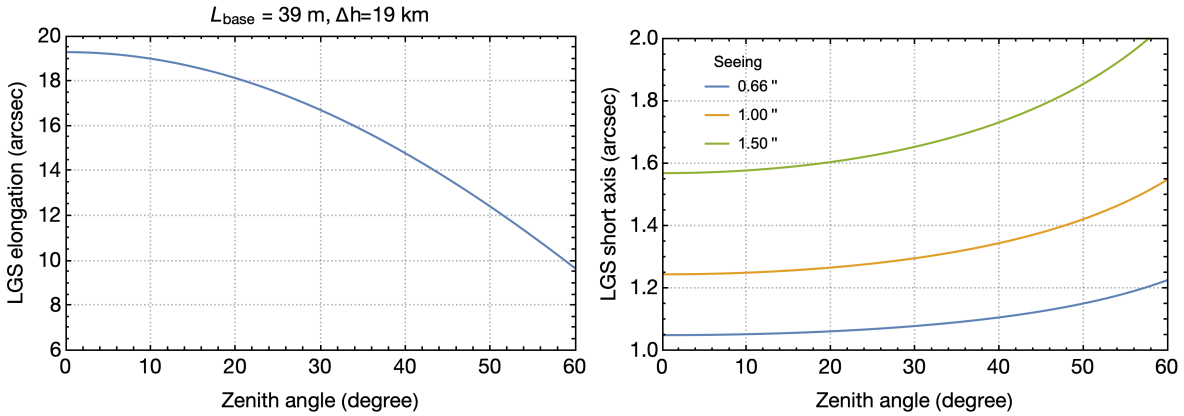

Figure 1. (Left) LGS elongation projection and (right) short axis angular size as a function of the zenith angle.

2. PROTOTYPE DESIGN

2.1 Optical train

The optical train is composed of three main parts: the source, the Spatial Light Modulator (SLM), and the Laser Guide Star detector module (LDM), as shown in Fig. 2.

The first source used in the experiment is a light emitting diode (LED) coupled with a $400\mu m$ core diameter multi-mode optical fiber, equivalent to ≈ 1" LGS (see section 2.2). This LED is a simple reliable solution with an homogeneous intensity over the pupil. This source was used for the characterization of the LDM, to acquire interaction matrices and reconstruct wavefronts. From that, we moved to an elongated source capable of created an equivalent LGS of 1" $\times$ 16"(see section 2.2).

Then, the light from the source is collimated by a lens of $f = 45mm$ focal length and $D = 24mm$ diameter which acts as the entrance pupil of the system, this value is found using the Helmotz invariant (see section 2.2).

The next step is the SLM (see section 3.1) that can be used either like a deformable mirror or to generate phase aberrations. The SLM screen size is 1920×1152 pixels with a pixel size $p = 9.2\mu m$, therefore the maximum

size of a round beam on the slm is given by $1152 \times 9.2\mu m \equiv 10.6mm$. The first pupil is conjugated on the SLM through an afocal lens system of magnification $m = 1/2.5$. The full pupil size on the SLM is $9.6mm$ over 1043 SLM pixels, 1 subaperture of the MLA sees 13×13 SLM pixels.

For optimal use of the SLM, the light must be polarized and monochromatic, therefore we have a spectral filter $589 \pm 4nm$ and a polarizer before the SLM.

The light is then conjugated on the MLA through an afocal lens system of magnification $m = 2.5$, the diameter of the light beam on the MLA is $24mm$ in the 80×80 lenslets configuration.

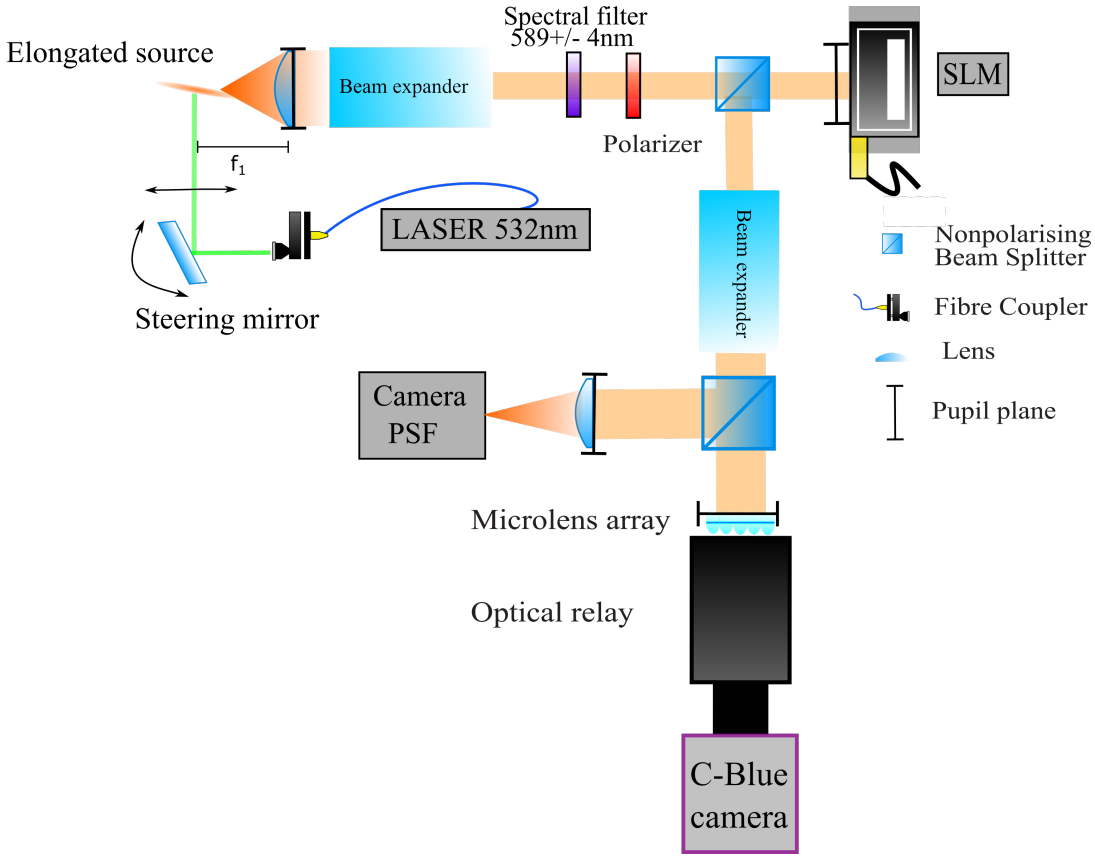

Figure 2. Optical scheme of the LGSS prototype bench.

2.2 Source: single and elongated spot

The laser guide star is a 3-D extended object with an evolving geometry depending on the laser beam size, sodium layer density distribution, and perspective of observation. We design a source assuming typical ELT observations at 30° zenith angle, a vertical altitude of the sodium layer centroid of 89.9 km above the telescope with a median vertical extension of 19 km, and a median LGS spot size of 1.08 arcsec corresponding to an object of 0.54 m in diameter.[6,7] The Smith-Helmholtz invariant is given by

$$\mathcal{H} = y \times \eta, \tag{2}$$

where y is the height the object and η the maximum angle between the optical axis and a ray passing through the object axial position and the telescope aperture. The angle η can be estimated as $\eta = \arctan(D_{\text{pupil}}/L_{\text{object}}/2)$, where $D_{\text{pupil}} = 39$ m and $L_{\text{object}} = 104$ km, which gives $\eta = 0.187$ mrad. Using $y = 0.27$ m we obtain $\mathcal{H} = 50.6 \times 10^{-6}$ meter rad.

Our system's entrance aperture lens is 24 mm diameter and the size of the scaled LGS object height is given by

$$y' = \frac{\mathcal{H}}{\arctan(D_{\text{pupil}}/f_{\text{lens}}/2)}, \tag{3}$$

where f_{lens} is the focal length of the lens. Figure 3 shows the required object size (diameter) of the scaled LGS spot as a function of the focal length.

The elongation of the scaled LGS ($\Delta h'$) can be obtained through the longitudinal magnification (M_{L}) defined in terms of the transverse magnification (M_{T}) as

$$\Delta h' = M_{\text{L}}\Delta h = M_{\text{T}}^2\Delta h = (y'/y)^2\ \Delta h, \tag{4}$$

which can be found as a function of the lens focal length in combination with Eq. 3. Figure 3 shows the diameter and length of the scaled LGS as a function of the focal length of a 24 mm diameter lens. The focal length is chosen among standard off-the-shelf components, minimizing the scaled elongation. Using $f_{\text{lens}} = 45$ mm a non-elongated source can be closely emulated coupling a light source into a multimode fiber with a core diameter of 400 μm. The realization of the elongated source is more tricky.

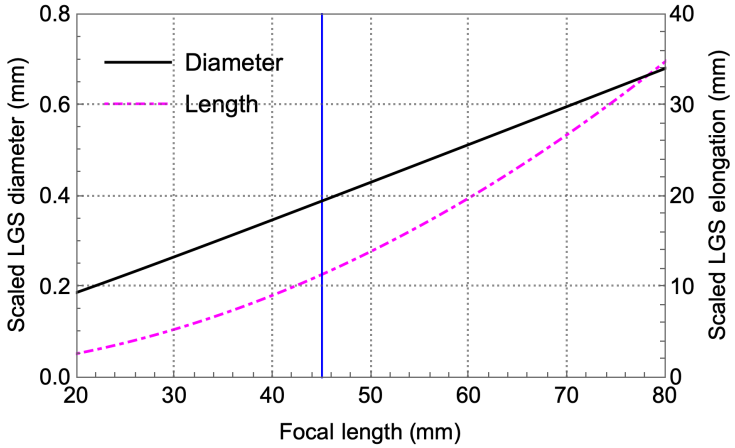

Figure 3. Diameter of a scaled LGS object (black solid line) and elongation of the scaled LGS (magenta dot-dashed line) as a function of the focal length for an aperture of 24 mm. At $f_{\text{lens}} = 45$ mm (blue vertical line), $y' = 388$ μm and $\Delta h' = 11.3$ mm.

Several approaches have been demonstrated elsewhere to emulate the effect of an elongated LGS in a Shack-Hartmann wavefront sensor. For example, in Ladière et al.[8] the elongation effect on a 29×29 subapertures wavefront sensor was reproduced by defocusing and refocusing a collimated beam during the integration time of the camera. A 40×40 subapertures prototype bench with an elongated source was presented by Patti et al.,[9] where the simulated LGS was realized by axially sweeping the position of an intensity-modulated fiber-coupled light source, resembling the sodium density profile during the integration time of the camera. An alternative design presented by Reeves et al.,[10] used a tube filled with a solution of Rhodamine 6G excited with a 532 nm laser light. The shape of the fluorescent laser beam through the solution was used as an elongated LGS source. Recently, Di Filippo et al.[11] emulated an elongated source as a line of white light emitted from an LED monitor on an alignment testbed of the INGOT wavefront sensor.

In this work we use a method that combines features from previous ones. Our design uses a capillary tube of 0.398 mm inner diameter and 32 mm length which we fill with a solution of Rhodamine 6G in ethylene glycol. A steering mirror is used to sweep a laser beam of 532 nm wavelength through the tube covering a section length of ≈11 mm, as calculated for an imaging system with a lens of $f_{\text{lens}} = 45$ mm and 24 mm diameter. Green light is absorbed in the medium and broadband light between ≈530 nm and ≈650 nm is emitted as fluorescence. To reproduce the elongated spots in the Shack-Hartmann, the laser beam must scan the tube at least during one integration time of the camera. The sweeping speed modulates the intensity of fluorescence and can be adjusted

to reproduce different sodium density profiles. The position of the tube in front of the lens is fixed and adjusted with an angle of 15° to simulate a single elongated spot. See Fig. 4 for an schematic of our design.

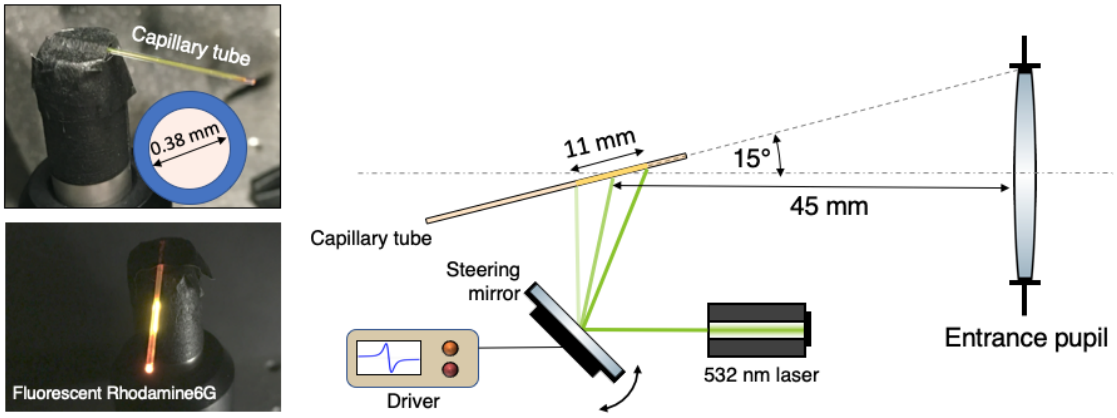

Figure 4. Schematic of our elongated source design.

Figure 5 shows the ellipticity of the spots over a grid of 73×73 subapertures in the LDM. The ellipticity is defined as $\varepsilon = (a+b)/b$, where a is the major axis, and b is the minor axis. A histogram for each axis is also presented showing that the non-elongated components remains around 1.4 pixels FWHM. while the elongated component varies from 1.4 px up to 6.5 px (or equivalently from 1 to 4.6 non-elongated spots).

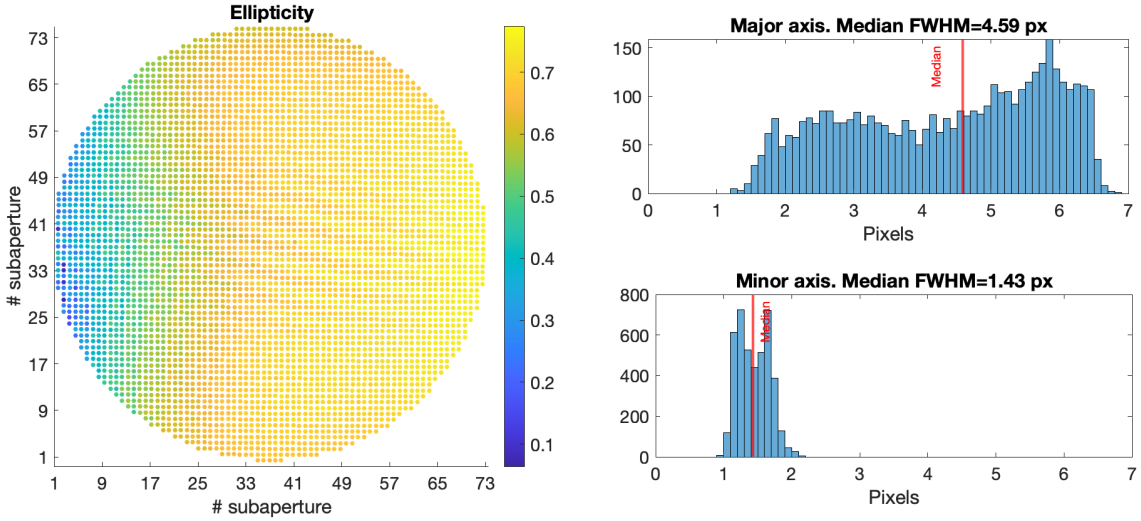

Figure 5. (Left) Ellipticity of the spots on each of the 73×73 subaperture of the LDM. (Right) Histograms of the minor and major axis for each spot.

2.3 Spatial light modulator

The SLM comes from Meadowlarks, model 1920x1152 XY Phase Series. It is a versatile tool, it can be used as a DM (see section 3.3) and to generate turbulences. To understand why we chose an SLM instead of a DM, we summarize in the following table some of the principals characteristics of the Meadowlarks SLM and a typical DM with a large number of actuators:

	SLM (1920x1152 XY Phase Series)	DM (64×64 actuators)
Cost	$\approx$ 20k€	$\approx$ 500k€
Pupil	10.59mm (pixel length=9μm)	93mm
Max phase amplitude	λ without phase wrap	up to $\approx 90\mu$m
Phase resolution	$\lambda/256$	sub-nm
Frequency	520Hz	up to 1kHz
Wavelength	monochromatic	large spectral acceptance
Polarization	linear	any polarization

The cost is one of the main reason to use a SLM. Also, the number of pixels 1920×1152 allows use to emulate a 80×80 DM with 13×13 SLM pixels per subapertures and add turbulences at the same time. Our source being a LGS, it is not a problem to use a monochromatic polarized incident beam on the SLM. We give further details on the SLM in the section 3.1.

2.4 LGS detection module

The Laser Guide Star Detector Module (LDM) is a Shack-Hartmann wavefront sensor consisting of an array of double lenslets, an optical relay and a detector camera. An optomechanical view of the LDM is shown in Fig. 6. This is a prototype for the Laser Guide Star System of HARMONI and it is designed to accept a 24 mm pupil on a microlens array of 84 lenslets over its diameter, providing a subaperture field of view of 15 arcsec projected on sky with 13 pixels side length per subaperture.

The microlens array prototype has been manufactured by AMUS. Our concept is based on a double microlens array where the second surface acts as a field lens. The double-lenslet has the advantage of creating a telecentric image and of reducing the steepest beam angle on the detector by half with respect to a classical lenslet. The microlens array is manufactured on a circular substrate of 30 mm in diameter made of fused silica ($n = 1.4584$ at 589 nm). The lenslets on both sides are identical and aligned within 10 μm. The shape of each lenslet is square with a spherical convex surface. The required lenslet pitch is 0.290 mm$\pm$0.005 mm with a central thickness is 3.5 mm$\pm$0.1 mm.

The relay is based on a preliminary design of the LDM from 2019. It has been developed to be manufactured with simple lenses in order to have an optical system readily available. It comprises six optical elements designed to provide a magnification of 1/2.52 and a pixel scale of 1.16 arcsec/pixel. No constraints in term of requirements on distortion, telecentricity have been defined. The goal of the relay is to conjugate the microlens array with a good image quality. The optics has been assembled using off-the-shelf components.

The detector is a Sony CMOS model IMX425LLJ on board of a C-BLUE One camera manufactured by First Light Imaging.[12] The detector array has 1604 $\times$ 1104 active pixels, each of which with a square size of 9.0 μm $\times$9.0 μm. The active pixels include an analog-to-digital converter of 8, 10, or 12-bits and global shutter read-out. The quantum efficiency reported by the manufacturer is 0.70 at 590 nm.

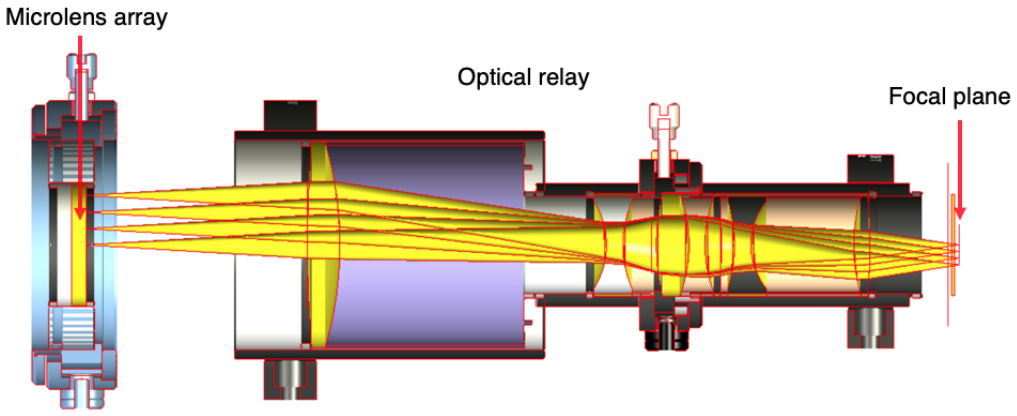

Figure 6. Optomechanical design of the Laser Guide Star Detector Module prototype. The overall length of the relay is about 150 mm.

2.5 Design summary

A summary of the design parameters of the bench is shown in the following table.

Table 1. Design parameters.

	Parameter	Comments
Source		
Non-elongated	0.40 mm diameter	Output of MM fiber
Elongated	0.38 mm x 11 mm	Capillar tube of Rhodamine 6G
Optical		
Entrance pupil	23.8 mm	
Field of view	-	
SLM pupil	10 mm	
Wavelength	590 nm	Band pass filtered with $\Delta\lambda = 10$ nm.
Polarization	Linear	Required for SLM. Use of polarizer.
LDM		
Lenslet array	84 x 84 lenslets	Over 30 mm diameter. Double lenslets.
Lenslet pitch	0.290 mm	Square lenslets.
Pupil size	24 mm	Partial illumination of lenslet array.
Relay magnification	1/2.52	Six elements relay.
Detector size	1604 x 1104 pixels	CMOS sensor
Pixel pitch	9 microns	
Sub-aperture size	13 x 13 pixels	
Sub-aperture FoV	16 arcsec	
Pixel scale	1.2 arcsec/pixel	
Source sampling	0.9 pixels FWHM	Assumes LGS spot of 1.08 arcsec.

3. CHARACTERIZATION OF THE SYSTEM

3.0.1 Lenslets characterization

Double-sided lenslet array are not common in adaptive optics and tests on the manufacturing and the performance of the lenslet array are necessary to identify any issue we can meet during the manufacturing and development of LGSS. The principle is shown in Fig. 7. A prototype has then been ordered to **AMUS** with the characteristics shown in the following table:

Parameter	Value	Comments
Lenslet pitch	$290 \pm 5\mu$m	Compliant (Amus report)
Radius of curvature	1.1 ± 0.04mm	Compliant Tested with WYKO profilometer
Lenslet central thickness	3.5 ± 0.1mm	Compliant (Amus report)
Lenslet number	84	Compliant (Amus report)
Pupil size on the full lenslet array	24.0mm	Compliant (Amus report)
Lenslet F number	8.645	

The verification of the MLA performance is based on measurement from **AMUS** and verification done at LAM with a WYKO microscope that allows to measure the radius of curvature of the surface. The verification has confirmed that the MLA was within the requirements except for the filling factor of the MLA and the quality of the transition area. We need to assess how critical it is for the LGSS design but for the prototype development these effects are acceptable.

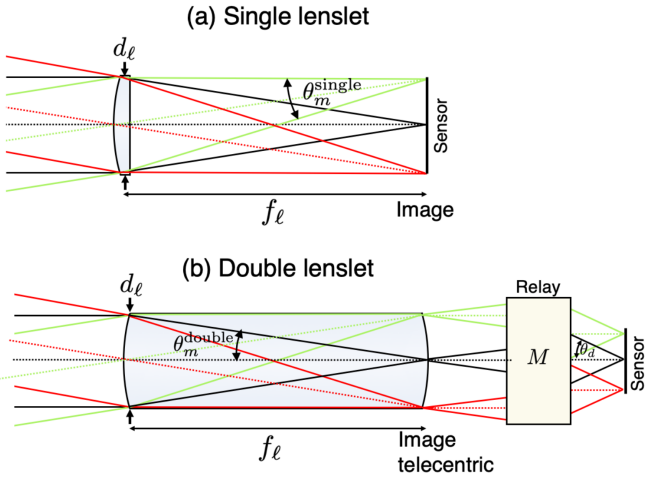

Figure 7. Figure from[13] .a) A single lenslet in front of the detector, b) double lenslet made with the same substrate, the field is created on the second surface of the lenslet to create a telecentric beam that can be re-imaged on the camera through a relay. This configuration reduces by half the incidence angle on the detector in comparison with the single lenslet.

3.0.2 Relay characterization

The relay presented here is prototype of the relay that will be on the final version of the LDM. The actual relay is developed by our colleagues of IPAG in Grenoble.[3] The general design of the final relay should be similar to the one presented here, but with better performances and with a different mechanical mount. We summarize the main characteristics of the relay in the following table:

Parameter	Value	Comments
Number of pixel / sub-aperture	12.75pixels	Best fit to a linear grid
Pixel scale	1.16" Pixel	
Relay magnification	$G = 2.52$	
FoV per microlens array	15.08"	
Number of lenses	6	Intermediate pupil plane

The relay has been aligned by adjusting the lenses with respect to the others. In particular we have the possiblity to optimise the optical performance of the relay by adjusting the 2 first lenses alignment with respect to the 4 other lenses. This is done by minimising the spots elongation over the pupil. We have also characterised the optical quality of the relay by measuring the Wavefront Error with a commercial Shack-Hartmann leading to a wavefront below 100 nm rms with the commercial lenses.

An important step in phase reconstruction with a SH is the knowledge of the reference grid. In the paraxial case, if the input wavefront is a non aberrated plane wave each focal points created by the MLA should fall in the center of a subaperture created by a linear grid on the detector.

However, in the current setup distortions are introduced by the relay. To quantify the distortion we use a simulation in which we create an array of telecentric beams along 1 axis at the position of the MLA (see fig. 8) and calculate their position on the detector after passing through the relay (see fig. 9). If there was no distortion, the position of the rays on the MLA and detector should overlap by adjusting the magnification. Instead, to obtain the plot in fig. 9 *a*), we adjust the magnification to remove quadratic contribution in the plot fig. 9 *b*), we find $M = 1/2.52$ and a 3^{rd} order component on the plot fig. 9 *b*) is still present.

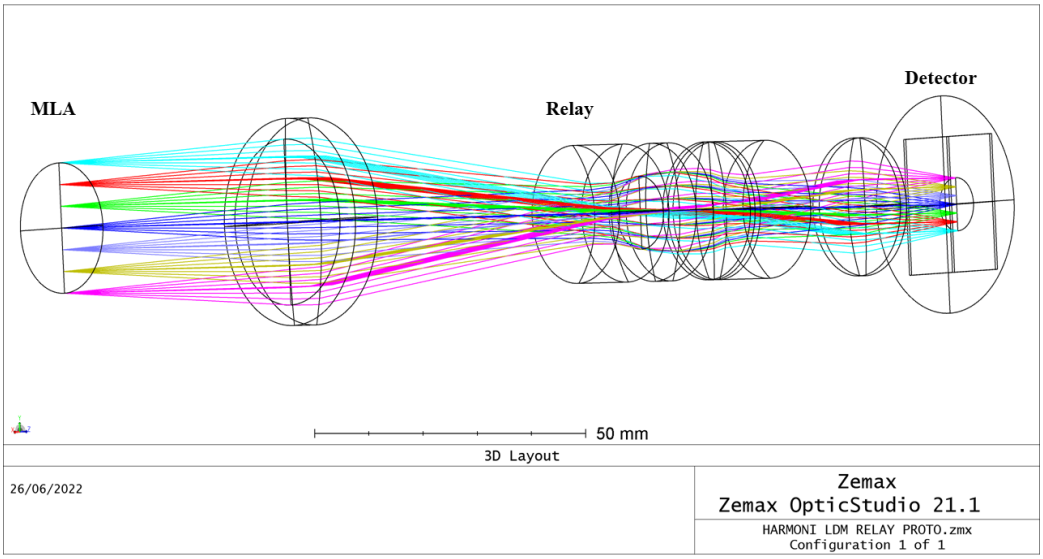

Figure 8. We inject equally spaced telecentric beams coming from the MLA along one axis and obtain their position on the detector through ray propagation using **OpticStudio**.

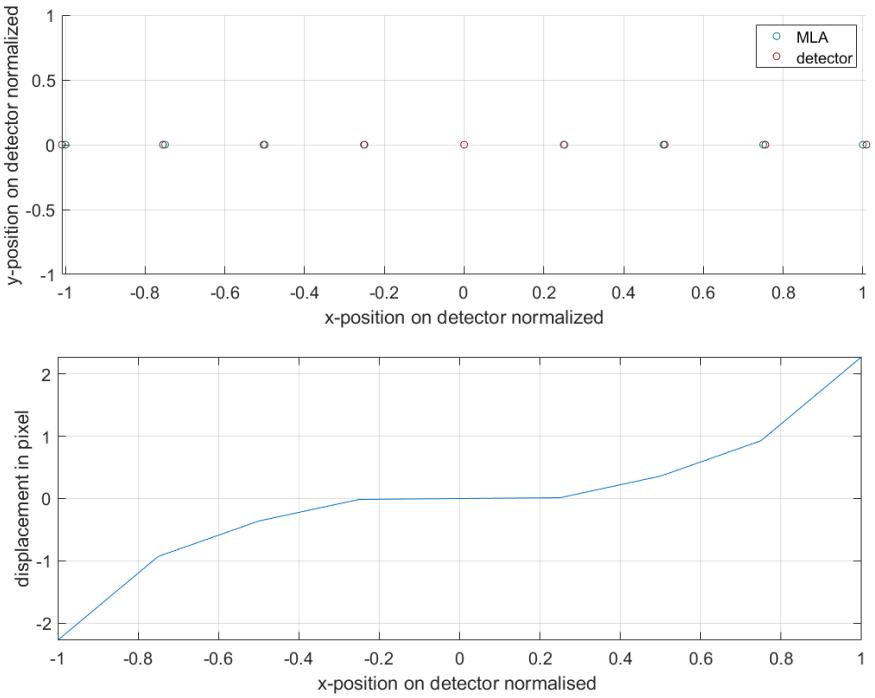

Figure 9. a) The blue cirles represents the position of telecentric beams on the MLA divided by the magnification, the red circles represents the position of the propagated telecentric beams through the relay. b) We plot the distance between the blue and red circles in unit of camera pixels.

Therefore, knowing the pitch of the MLA $s_{\text{lenslet}} = 290\mu$m, the pixel size of the dectector $s_{\text{pixel detector}} = 9\mu$m and the magnification, we can calculate the size of a subaperture on the detector, $s_{\text{subaperture}} = 290/2.52/9 = 12.78$pixels. To confirm experimentally, we fitted a linear grid to the slopes by minimizing the distance between the linear grid and the measured slopes, and we obtained $s_{\text{subaperture}} = 12.78$ pixels. In conclusion, the relay

creates distortions but we can find a linear grid where all the slopes fit reasonably, i.e. with a maximum of ≈ 2 pixels displacement in between the linear grid center and the distorted position of the spot. Given that $s_{\text{subaperture}} = 12.78$ pixels, this displacement can be absorbed when we acquire the reference slopes.

3.0.3 Camera characterization

The large number of subapertures to sample the ELT pupil and the required field of view per subaperture to minimize truncation of elongated spots, leads to a detector design with >1000 pixels across. In addition, the detector must have a very low read-out noise and must operate at a frame rate of 500 Hz. A commercial solution employing a complementary-metal-oxide-semiconductor (CMOS) technology was identified, which represents a change with respect to classical charge-couple device (CCD) detectors used in LGS wavefront sensors. We have performed a detailed study on the performance of the Sony CMOS sensor model IMX425LLJ on board of a C-BLUE One camera manufactured by First Light Imaging for LGS wavefront sensing.[12] We present here a few key findings, while we let the reader refer to Ke and Pedreros *et al.*[13] for more details.

The photon transfer curve (PTC) method was employed to characterize the electron to analog-to-digital units (ADU) conversion gain K, the read-out noise σ_{RON}, and the full-well capacity S_{FW} of the sensor. Figure 10 (left) shows the PTC measured over a square area of 100×100 pixels. Internal amplification gains in the camera are settable and they were set at its maximum sensitivity. The estimated parameters obtained from the PTC curve are $K = 0.2473 \pm 0.012\ e^-/\text{ADU}$, $\sigma_{\text{RON}} = 3.05 \pm 0.15\ e^-$, and $S_{\text{FW}} = 931/e^-$.

Another peculiar characteristic of the CMOS sensor is their sensitivity dependence to the incoming light angle of incidence. We measured the sensor response to a collimated beam at different incidence angles and in several rotation planes of the sensor. Figure 10 (right) shows the normalized response of the camera with respect to normal incidence. A decrease response towards oblique incidence imply a lower photon to electron conversion efficiency, which decreases the optical throughput of the system. For this reason, the wavefront sensor is designed maximizing the incident beam focal ratio. In the current LDM prototype design, the side beam F-number on the sensor is $f/3.4$ leading to an angular response efficiency of 95%. We encourage the reader to refer to Ke and Pedreros *et al.*[13] for additional calculations and information of this effect.

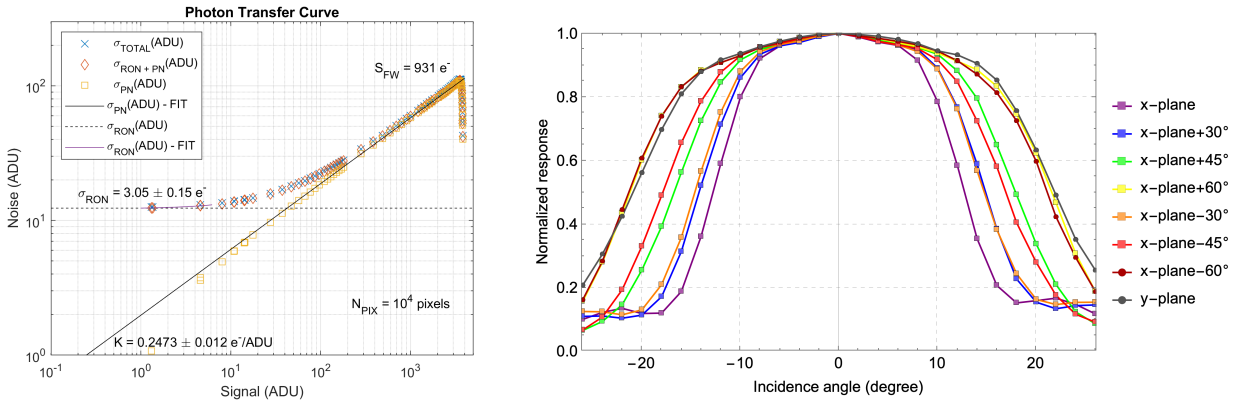

Figure 10. (Left) Photon transfer curve of the CMOS sensor in the most sensitive configuration. (Right) Profiles of the angular response with respect to normal incidence, in several rotation planes.

3.1 Spatial light modulator

In this section, we present the characterization of the time response and the limitations of the SLM.

3.1.1 SLM time response

An other interesting feature of this SLM is the fast time response, the constructor gives a frequency of 550Hz at $\lambda = 635$nm. To confirm that value, we loaded a phase map of striped on the SLM, then a fast photodiode is placed in a focal plane after the SLM to check the speed of intensity transfer between the zero and first order created by the grid (see figure 13).

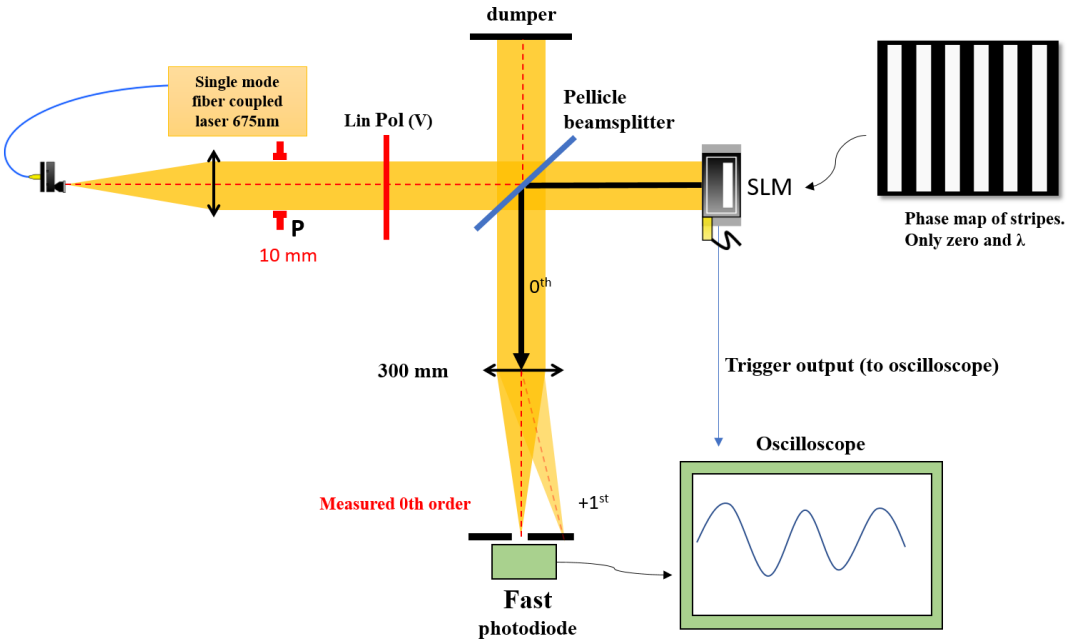

Figure 11. Setup of the SLM time response test.

We present here the result on the oscilloscope:

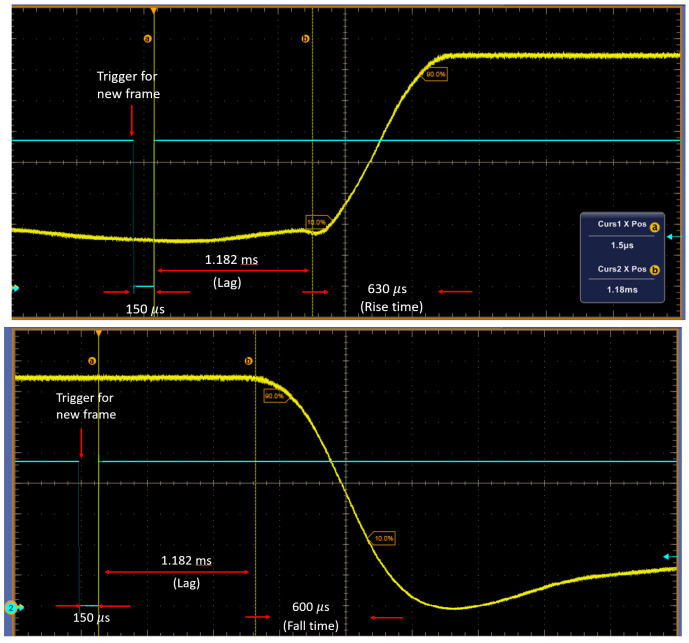

Figure 12. (Top) We start with the phase map of stripes then we upload a flat phase map, therefore the intensity is rising as we measure the 0^{th} order (Bottom) We start with a flat phase map then we upload the phase map of stripes, therefore the intensity of the 0^{th} order is dropping.

We display two signals on the oscilloscope, the signal from the photodiode (yellow) and the signal from the SLM trigger (blue). After the trigger signal of 150 ms, the phase map is loaded on the SLM, it introduces an

unavoidable lag of 1.18 ms between the flipping of memory bank and loading the image. Finally, the time for the liquid crystal to settle is ≈ 600ms.

$$\text{framerate} = \frac{1}{\text{trigger delay} + \text{loading phase map delay} + \text{liquid crystal lag}} = 520\text{Hz}, \tag{5}$$

Then, we create a continuous sequence where we alternate between the stripes and the flat phase map. The result is that we can load images at a rate of 837Hz (see fig. 13). However, these measurements are done with a simple pattern and we measure the global phase map effect, an other test would be to use the SLM in an AO closed loop and see how fast can we compensate for a turbulent wavefront by checking the PSF quality.

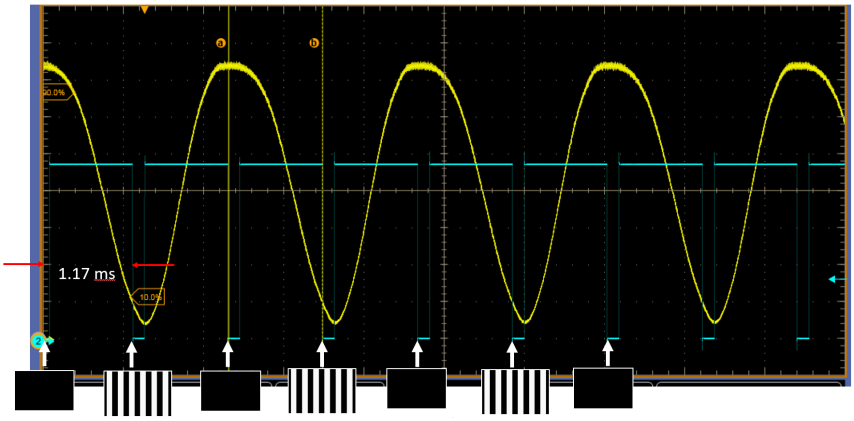

Figure 13. Continuous mode.

3.1.2 Phase wrap limitation

The principle of phase wrapping on a SLM is equivalent to the principle of a Fresnel lens,[14] it takes advantages that for a wave its phase is defined $\mod 2\pi$. For example, if we want a slope that goes from 0λ to 2λ over 13 pixels on the SLM (number of SLM pixels per SH subaperture), we have to wrap the phase because each pixel has a maximum phase shift of 1λ, therefore in fig. 14 the slope seen by the is $2\lambda/13$pixels. The largest slope that can be created on the SLM is given by the number of pixels to sample the phase map pattern. In fig. 14, we have 7 pixels to create a slope between 0 and λ, the slope is well sampled.

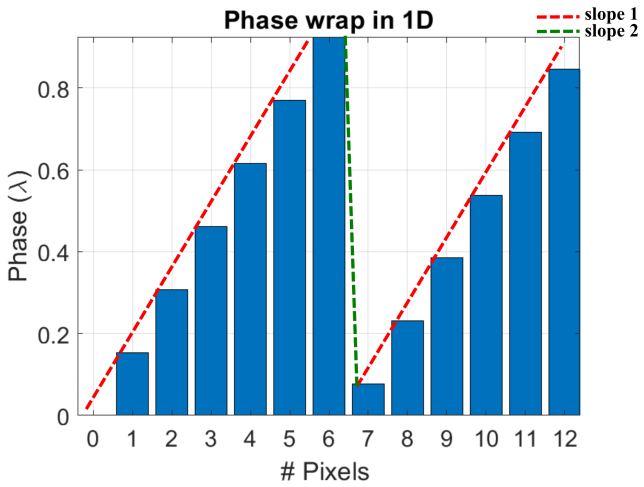

Figure 14. 1D phase wrapped tilt of 2λ over 13 pixels on the SLM.

To test that hypothesis, we applied a phase wrapped tilt with the SLM, and we see on fig. 15 that if we generate a tilt bigger than 3λ, 2 spots appear on the detector, this come from the fact that 2 slopes are seen by the light fig. 16. In other word, the situation becomes symmetrical for the incoming wavefront, this represent the fundamental limit of the SLM.

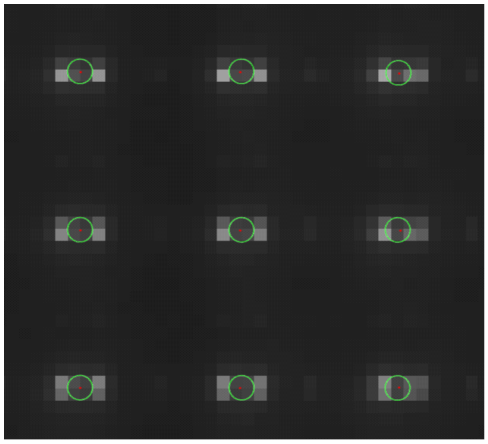

Figure 15. PSF of SH, each red dot represents the center of a subaperture and the green circle the COG of that subaperture. Here we observe 2 spots for one subaperture due to the phase wrapping.

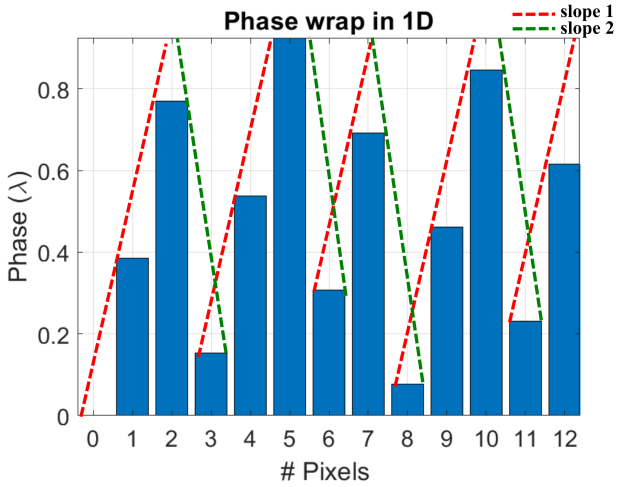

Figure 16. 1D phase wrapped tilt of 5λ over 13 pixels on the SLM. The incoming wavefront sees 2 different slopes.

An other limit of the SLM is that the phase wrapping generates intensity inhomogeneities in the pupil plane, see fig. 17. To acquire the image displayed on fig. 17, we removed the MLA and relay, then placed the C-Blue camera (see fig.2) in the pupil plane (MLA plane).

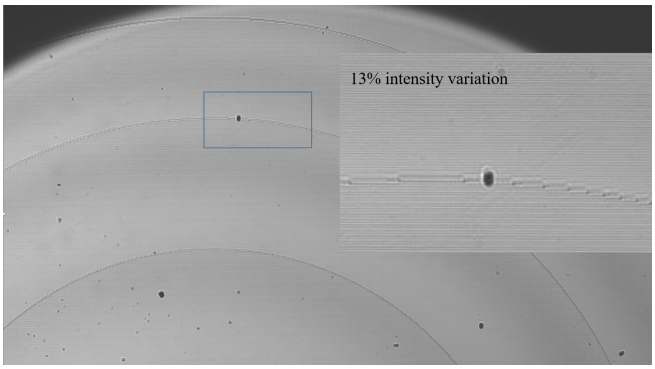

Figure 17. Direct image of a section of the pupil plane with a phase wrapped phase map pattern on the SLM.

The original phase map loaded on the SLM is a phase wrapped focus, and we observed intensity variations where the focus is phase wrapped. We think that is due to diffraction effects because of the SLM pixel having a fill factor $< 100\%$. Also, the input light is not perfectly monochromatic and the liquid crystal (LC) being birefringent, the delay introduced by the LC is $\propto \frac{1}{\lambda}$, therefore the light is not properly phase wrapped for all the wavelength.

3.1.3 Phase linearity - Lookup Table

The linearity of the output phase versus the input grayscale level must be calibrated before using the SLM. The linearity depends on the light wavelength, temperature of the device, and other system parameters. The lookup table (LUT) that linearize the output phase must be calibrated at the operation conditions of the SLM. The calibration setup is similar to the one shown in Fig. 13 and the procedure is the following. The high diffraction orders owing to the backplane pixel structure are filtered out and only the zeroth order beam is focalized. A photodiode is placed behind a pinhole to measure only the first diffraction order when a pattern of stripes acting as a grating is applied to the SLM. The low grayscale level is held at zero and the high grayscale level in this pattern is increased in unitary steps from 0 to 255. At the same time the signal from the photodiode, which is proportional to the intensity of diffracted light on multiple slits, is measured. An example of a signal vs grayscale curve is shown in Fig. 18. The signal between two consecutive minima corresponding to a phase change of 2π is processed to build the lookup table that linearize the output phase. In this case we obtain a "global" LUT as the full SLM surface is illuminated. The *diffractive calibration* method can be repeated on sub-areas of the SLM to obtain "regional" LUTs, minimizing the spatial non-linearities. Alternatively, the signal from the zero order can be measured, although one expect the opposite behaviour as the first-order measurement (2π phase in a grayscale interval between two maxima).

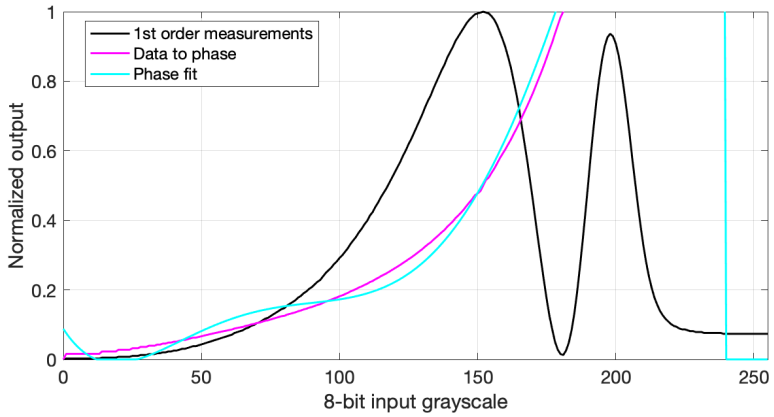

Figure 18. Signal from the photodiode as a function of the grayscale levels in the stripe pattern and grasycale to phase conversion.

3.2 WFS linearity and sensitivity

In this section we present the linearity response of the LDM. In other words, we apply a tilt in the SLM pupil plane (see fig. 2) which is translating the slopes in each subapertures, then we verify that the relation between the slope displacement and the tilt is linear. To do so, we use a steering mirror instead of the SLM capable of creating a larger tilt. The tilt could be created by the SLM but its amplitude in phase is limited (see section section 3.1).

3.2.1 Correspondence between phase and COG displacement

The information given by the LDM is a vector containing all the COGs coordinate in pixels. However, we need to know what is the phase. To do so we can first calculate the COG displacement D_{COG} created by a phase shift of λ:

$$D_{COG} = \frac{\lambda}{D} \times f \times M \tag{6}$$

Where $\lambda = 589$nm, D is the size of a microlens 290μm, f the focal length of a microlens and the magnification $M = 1/2.52$. We obtain $D_{COG} = 2.0557\mu$m, which correspond to 0.242 pixel of the C-blue camera. Finally we can write the phase as a function of the pixels displacement:

$$\phi_{\text{tilt}} = 4.13 \times D_{\text{COG}}. \tag{7}$$

where ϕ is the Zernike coefficient for the tilt given as a multiple of λ.

3.2.2 Linearity measurements

The rotation of the steering mirror creates a tilt, consequently knowing the size of the pupil on the steering mirror and its angle of rotation, we can fin a relation between the angle of rotation and the value of the tilt in terms of phase, there are multiple ways to describe the phase, in radians, as an OPD, or as a multiple of λ with $2\pi(\text{rad})\widehat{=}\lambda$. In this section we use the latter, and we divide this value by the number of subapertures over the full pupil along one axis, here this number is $N_{\text{sub}} = 73$, as a result we know the phase seen by each subaperture. On the result fig. 19, the left plot gives the relation between the tilt created by the steering mirror (horizontal axis) and the tilt measured by the LDM (vertical axis). The different lines represent the different subapertures. The right plot is an histogram of the slope coefficient for each subapertures. It the linearity coefficient is equal 1, it means that the value of the tilt created with the steering mirror corresponds the same tilt value measurement by the LDM. Moreover, The residual part of the linear fitting is negligible.

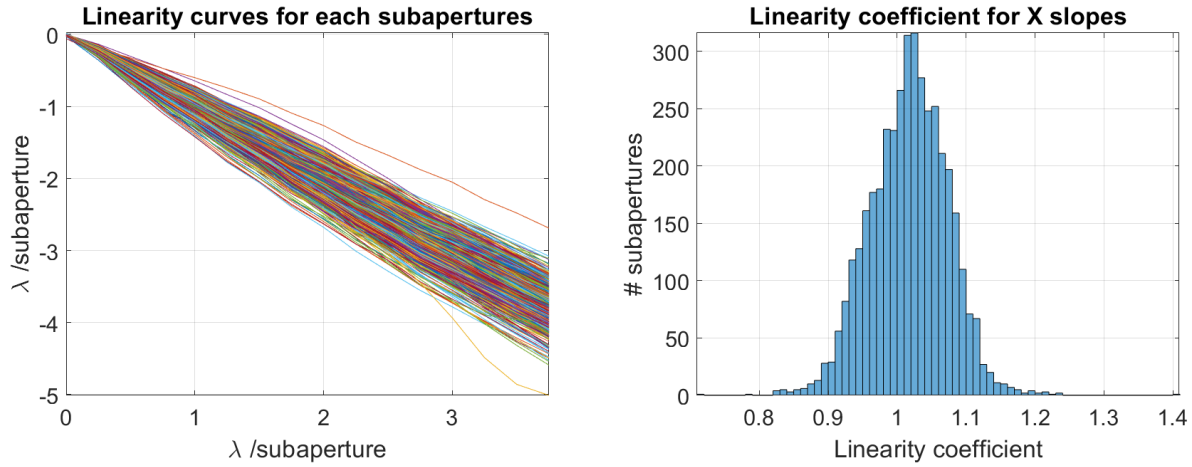

Figure 19. (Left) Tilt created by the steering mirror (horizontal axis) VS the tilt measured by the LDM (vertical axis). (Right) Histogram of the slope coefficient for each subapertures .

3.2.3 Sensitivity

The error on the determination of a slope position depends mainly on the photon flux in each subaperture, the region of interest to the center of gravity (COG), the read out noise of the camera. This characterisation has been done in a paper[13] by Ke, Pedreros et al.

Our first objective is to obtain clean interaction matrices (IM) to characterize the AO performances (see section 3.4). Therefore as a first step, we are working in a high photon regime > 8000 photons/subaperture/frame, in this regime the limitation is the photon noise. In fig. 20, we present the temporal standard deviation for each subaperture (each pixel on the plot represent a subaperture) over 10 images, the image acquisition framerate is at 200Hz.

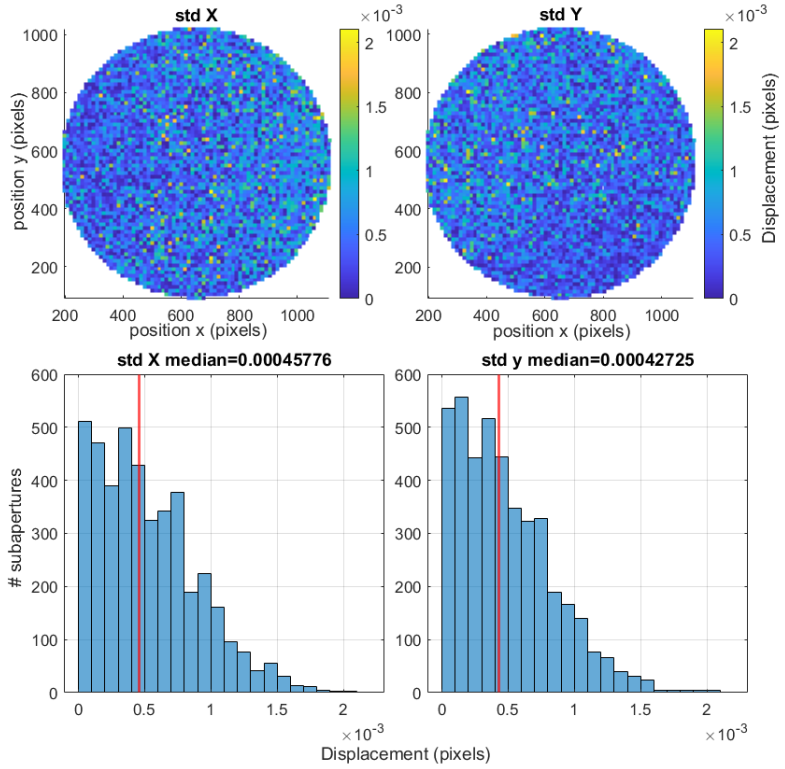

Figure 20. (Left) Temporal standart deviation of the $x-$axis COG measurement for each subaperture with the corresponding histogram below. (Right) Same as (left) for the $y-$axis.

The median error for each subaperture is $\approx 10^{-3}$ pixels. If we consider that each subaperture sees only tip/tilt, it corresponds to an error of $\phi_{\text{error}} \approx 2$nm. The next step will be to reduces the photons flux to 300 photons/subaperture/frame to approach the on-sky regime and see its influence on the reconstruction.

3.3 The SLM as a DM

In AO, the DM is the part that corrects the distorted wavefront of the light coming from space, to do so, a thin membrane is deformed by small actuators pushing or pulling the membrane. These deformations change the local OPD of the incoming wavefront according to the so called influence function of the actuator. These function depends on each DM, but can be modeled as first approximation by a 2D gaussian surface. On the other hand, a SLM is an array of pixels, each of these are independent and we can assign a piston between 0 and λ with a resolution of $\lambda/256$. The influence functions of M4 can be defined on the SLM and projected on M1 in the pupil plane to simulate the DM, see fig. 21.

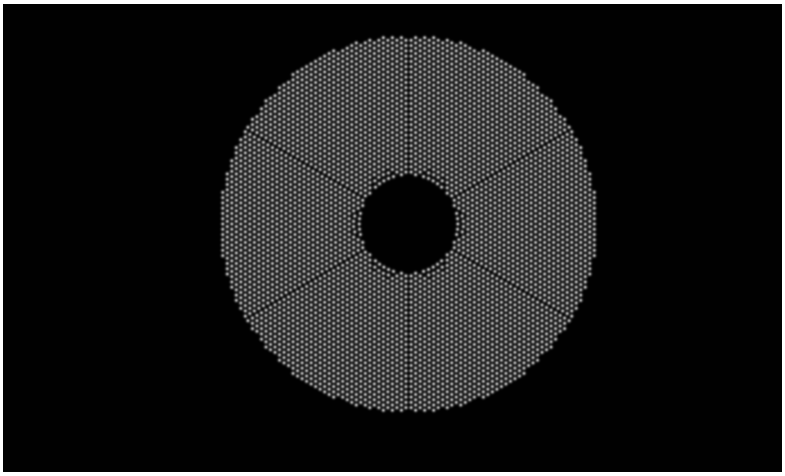

Figure 21. All the influence functions of M4 projected on the pupil M1 of the ELT. The FWHM of the influence function is reduced to have a better view of their positions.

Therefore, to emulate the influence function (see fig. 22), we take as first approximation a 2D Gaussian surface and add an offset of half the maximum phase amplitude of an SLM pixel, that is $\lambda/2$. Thereby, the influence function have the same base like on the membrane of a DM.

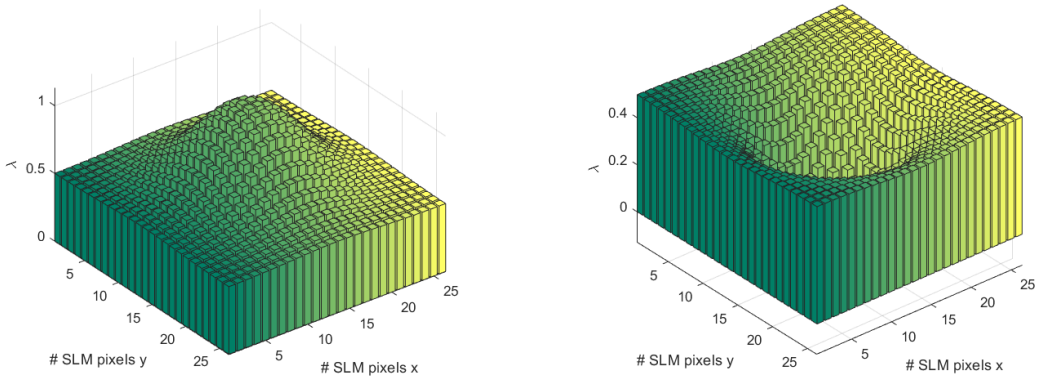

Figure 22. (Left) Actuator push on a SLM. (Right) Actuator pull on a SLM.

3.4 Interaction matrix and reconstruction

In AO systems, the aim is to measure turbulent wavefronts and send the correct information to a DM to compensate for those turbulences. For a SH, the connection between the measured slopes and the wavefront is a $N_{slopes} \times N_{actuators}$ interaction matrix[15] :

$$B = \begin{bmatrix} x_1^1 & x_1^2 & ... & x_1^n \\ \vdots & \vdots & ... & \vdots \\ x_n^1 & x_n^2 & ... & x_n^n \\ y_1^1 & y_1^2 & ... & y_1^n \\ \vdots & \vdots & ... & \vdots \\ y_n^1 & y_n^2 & ... & y_n^n. \end{bmatrix} \tag{8}$$

To fill the IM, we push on each actuators and save the corresponding slopes in a column vector $u_i^j = [x_1^j, ...x_n^j, y_1^j, ..., y_n^j]$, where j corresponds to the j^{th} actuator, and i corresponds to the i^{th} slope. Here we choose

to save first the x axis slopes, then the y axis, this choice is arbitrary. We can summarize the connection between the slopes and the actuators by:

$$s = B\phi, \tag{9}$$

where ϕ is a vector containing the coefficients that you need to apply on the actuators to reconstruct the phase map corresponding to the slope vector $\mathbf{s}$. However, in a AO system you need the actuators coefficients knowing the slopes, therefore B needs to be inverted using pseudo-inversion[15] because B is a non-square matrix. The pseudo-inverse of B is called the command matrix, and we can write:

$$\phi = B^{-1}s, \tag{10}$$

The difference here is that we are using a SLM instead of DM. The advantage of the SLM is that we can simulate a variety of DM geometry with different influence functions. In our study we choose first to study a DM with 4452 actuators, therefore we obtain 8502 slopes. The influence functions are gaussian functions with $\sigma = 6$ SLM pixels, and distributed on a regular grid (Fried geometry). To obtain the IM, we print each influence function on the SLM and save the corresponding slopes as a column of B (see fig. 23).

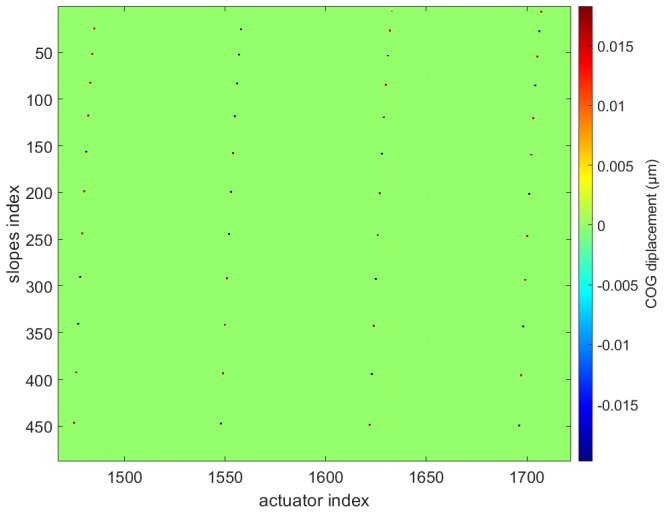

Figure 23. Subset of a 8502×4452 IM.

From the IM we use pseudo-inversion to obtain the command matrix and reconstruct wavefront, as an example we upload a Zernike mode Z_{12}^{-4} with a coefficient of 7λ on the SLM:

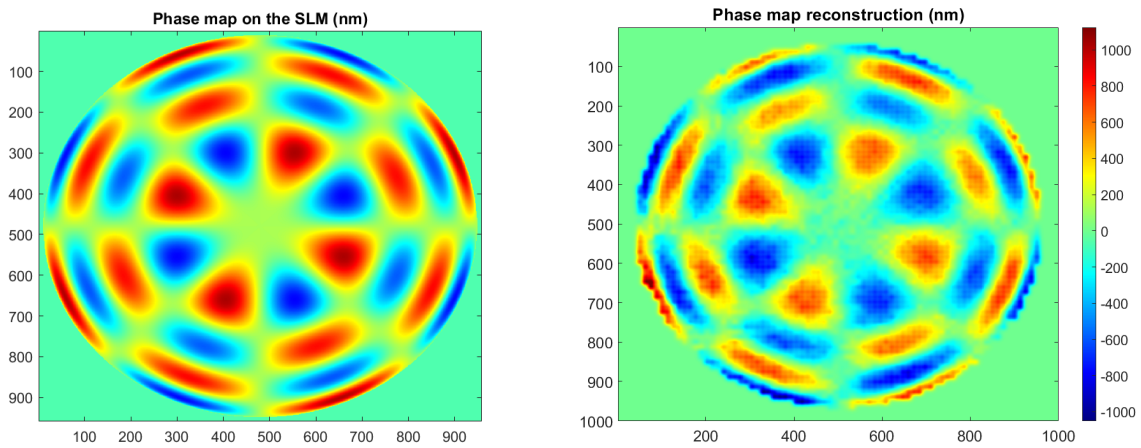

Figure 24. (Left) The original phase map loaded on the SLM. (Right) The reconstruction through the LDM .

We also carried simulations, using a geometrical synthetic interaction matrix and including the error on the slope measurements given in section 3.2.3.

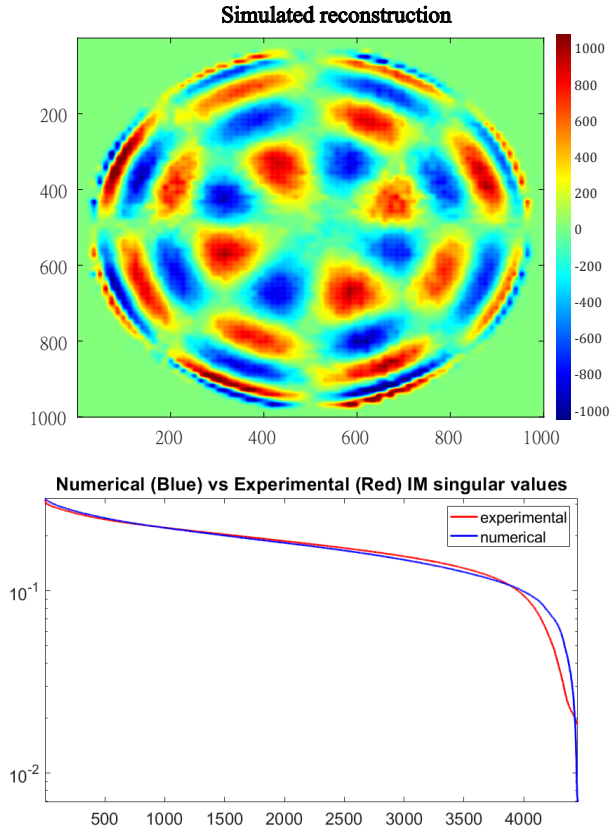

Figure 25. (Top) Simulation of reconstruction using gemetrical synthetic IM. (Bottom) Singular values of the experimental and synthetic IMs.

We present the singular values of the LDM on fig. 25, the singular value distributions for the simulation and experimental data are similar. The highest eigen modes of the LDM also represent the highest frequency mode,

in the simulation the highest modes are better seen than the experimental ones.

We also give preliminary results of phase map reconstruction with an interaction matrix done with **ESO** influence function and the M4 geometry:

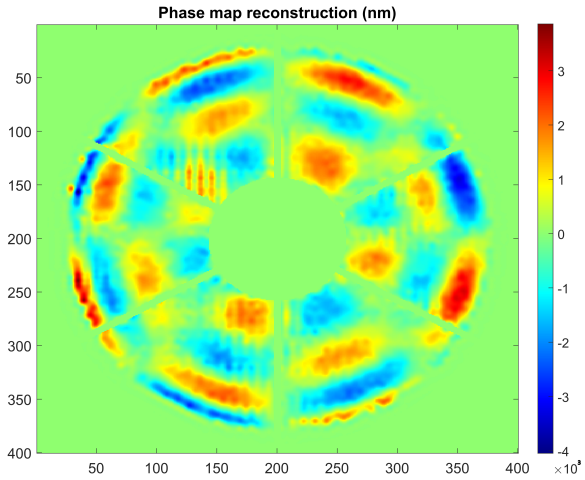

Figure 26. Reconstruction of a Zernike phase map loaded on the SLM in the M4 configuration.

Some ripples are present in fig. 26, this is probably due to the conditioning of the interaction matrix. The geometry of M4 in the pupil is more complex than the Fried geometry, therefore the choice of the useful actuators can influence more the IM and therefore the reconstruction. Next step will be to improve the reconstruction in that geometry with a better IM conditioning.

In conclusion, we reached our first objective which was to show the capability of the prototype bench to reconstruct a phase map generated by the SLM. From that point, we want to test the limit of this bench in terms of phase map reconstruction in more realistic conditions, i.e. with less photon flux, elongated spots, M4 geometry.

3.4.1 The closed loop regime

We closed the loop on a static aberration, the prototype does not have a RTC and therefore the closed loop is done at low framerate. We present the first results in the following figure:

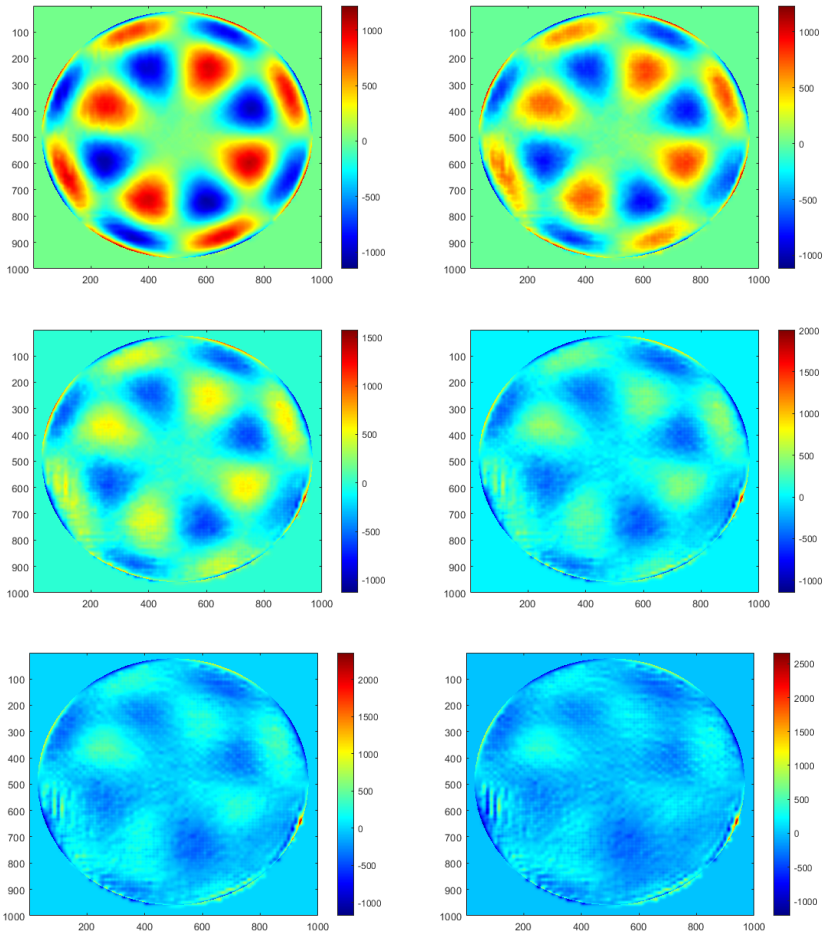

Figure 27. We diplay a Zernike pattern on the SLM and we close the loop over 6 iterations.

And the corresponding RMS values in nm in the following figure:

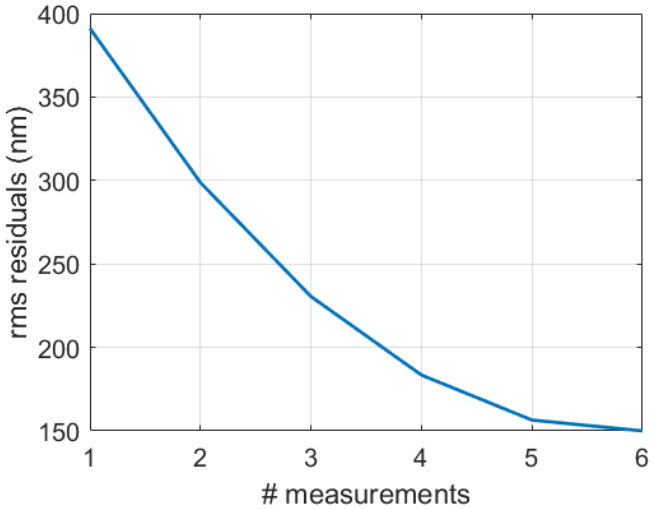

Figure 28. The corresponding **RMS** value for each iterations of the closed loop.

4. CONCLUSIONS AND OUTLOOK

We achieved important steps in the conceptions of a full scale realistic LGS WFS for HARMONI.

- We characterized the important elements of the LDM. We demonstrated the viability to integrate a CMOS sensor in an adaptive optics system[13] . We characterized the prototype relay and the MLA . We obtained the first phase map reconstruction with 73×73 subapertures with a non elongated source, we were able to close a loop in that configuration. The next step will be to close a loop with the M4 geometry.
- We proposed an innovative solution to simulate elongated source with different intensity distributions. This will allow us to confirm the simulations[2] of phase reconstruction with truncated spots. The next step will be to perform a finer characterization of the elongated spots.
- We demonstrated the capacities of the SLM to emulate the M4 DM and open new perspectives to test adaptive optics concepts such as super resolution[4] or misregistration algorithm.

In conclusion, this bench is a versatile tool to test AO concepts with elongated/non elongated spot, a large number of subapertures, a range of different DM geometry and influence functions.

5. ACKNOWLEDGEMENTS

This project received funding from the European Union's Horizon 2020 research and innovation programme under the Marie Sklodowska-Curie grant agreement No 893150. This work also benefited from the support of the WOLF project ANR-18-CE31-0018 of the French National Research Agency (ANR) ,APPLY (ANR-19-CE31-0011), LabEx FOCUS (ANR-11-LABX-0013), and the Programme Investissement Avenir F-CELT (ANR-21-ESRE-0008). This document has been prepared as part of the activities of OPTICON H2020 (2017-2020) Work Package 1 (Calibration and test tools for AO assisted E-ELT instruments). OPTICON is supported by the Horizon 2020 Framework Programme of the European Commission's (Grant number 730890). This work was supported by the Action Spécifique Haute Résolution Angulaire (ASHRA) of CNRS/INSU co-funded by CNES, the ECOS-CONYCIT France-Chile cooperation (C20E02), the ORP H2020 Framework Programme of the European Commission's (Grant number 101004719) and STIC AmSud (21-STIC-09).

REFERENCES

[1] Thatte, N., Tecza, M., Schnetler, H., Neichel, B., Melotte, D., Fusco, T., Ferraro-Wood, V., Clarke, F., Bryson, I., O'Brien, K., Mateo, M., Garcia Lorenzo, B., Evans, C., Bouché, N., Arribas, S., and HARMONI Consortium, "HARMONI: the ELT's First-Light Near-infrared and Visible Integral Field Spectrograph," *The Messenger* **182**, 7–12 (Mar. 2021).

[2] Neichel, B., Fusco, T., Sauvage, J.-F., Correia, C., Dohlen, K., El-Hadi, K., Blanco, L., Schwartz, N., Clarke, F., Thatte, N. A., Tecza, M., Paufique, J., Vernet, J., Louarn, M. L., Hammersley, P., Gach, J.-L., Pascal, S., Vola, P., Petit, C., Conan, J.-M., Carlotti, A., Vérinaud, C., Schnetler, H., Bryson, I., Morris, T., Myers, R., Hugot, E., Gallie, A. M., and Henry, D. M., "The adaptive optics modes for HARMONI: from Classical to Laser Assisted Tomographic AO," in [*Adaptive Optics Systems V*], Marchetti, E., Close, L. M., and Véran, J.-P., eds., **9909**, 92 – 106, International Society for Optics and Photonics, SPIE (2016).

[3] Costille, A., "HARMONI at ELT: Designing a laser guide star wavefront sensor for the ELT," International Society for Optics and Photonics, Proceeding SPIE (2022).

[4] Fusco, T., Agapito, G., Neichel, B., Oberti, S., Correia, C. M., Haguenauer, P., Plantet, C., Pedreros Bustos, F., Ke, Z., Costille, A., Jouve, P., Busoni, L., and Esposito, S., "Key wavefront sensors features for laser-assisted tomographic adaptive optics systems on the ELT," *Journal of Astronomical Telescopes, Instruments, and Systems* **8**(2), 021514 (2022).

[5] Pfrommer, T. and Hickson, P., "High resolution mesospheric sodium properties for adaptive optics applications," **565**, A102 (May 2014).

[6] Holzlöhner, R., Bonaccini Calia, D., and Hackenberg, W., "Physical optics modeling and optimization of laser guide star propagation," in [*Adaptive Optics Systems*], Hubin, N., Max, C. E., and Wizinowich, P. L., eds., *Society of Photo-Optical Instrumentation Engineers (SPIE) Conference Series* **7015**, 701521 (July 2008).

[7] Moussaoui, N., Clemesha, B. R., Holzlöhner, R., Simonich, D. M., Bonaccini Calia, D., Hackenberg, W., and Batista, P. P., "Statistics of the sodium layer parameters at low geographic latitude and its impact on adaptive-optics sodium laser guide star characteristics," *A&A* **511**, A31 (2 2010).

[8] Lardière, O., Conan, R., Bradley, C., Jackson, K., and Herriot, G., "A laser guide star wavefront sensor bench demonstrator for tmt," *Opt. Express* **16**, 5527–5543 (Apr 2008).

[9] Patti, M., Lombini, M., Schreiber, L., Bregoli, G., Arcidiacono, C., Cosentino, G., Diolaiti, E., and Foppiani, I., "Prototype of a laser guide star wavefront sensor for the Extremely Large Telescope," **477**, 539–547 (June 2018).

[10] Reeves, A. P., Myers, R. M., Morris, T. J., Basden, A. G., Bharmal, N. A., Rolt, S., Bramall, D. G., Dipper, N. A., and Younger, E. J., "DRAGON, the Durham real-time, tomographic adaptive optics test bench: progress and results," in [*Adaptive Optics Systems IV*], Marchetti, E., Close, L. M., and Véran, J.-P., eds., **9148**, 1903 – 1912, International Society for Optics and Photonics, SPIE (2014).

[11] Di Filippo, S., Greggio, D., Bergomi, M., Radhakrishnan, K., Portaluri, E., Viotto, V., Arcidiacono, C., Magrin, D., Marafatto, L., Dima, M., Ragazzoni, R., Janin-Potiron, P., Schatz, L., Neichel, B., Fauvarque, O., and Fusco, T., "INGOT Wavefront Sensor: from the optical design to a preliminary laboratory test," in [*6th International Conference on Adaptive Optics for Extremely Large Telescopes*], AO4ELT, Quebec City, Canada (June 2019).

[12] Gach, J.-L., Boutolleau, D., Brun, C., Carmignani, T., Clop, F., Feautrier, P., Florentin, M., Pettigiani, J., Stadler, E., Tugnoli, J., and Wanwanscappel, Y., "C-BLUE One: a new CMOS camera dedicated for laser guide star wavefront sensing on ELTs," in [*Adaptive Optics Systems VII*], Schreiber, L., Schmidt, D., and Vernet, E., eds., **11448**, International Society for Optics and Photonics, SPIE (2020).

[13] Ke, Z., Pedreros Bustos, F., Atwood, J., Costille, A., Dohlen, K., Hadi, K. E., Gach, J.-L., Herriot, G., Hubert, Z., Jouve, P., Rabou, P., Veŕan, J.-P., Wang, L., Fusco, T., and Neichel, B., "Performance of a complementary metal-oxide-semiconductor sensor for laser guide star wavefront sensing," *Journal of Astronomical Telescopes, Instruments, and Systems* **8**(2), 021511 (2022).

[14] Goodman, J. W., "Introduction to fourier optics," *Introduction to Fourier optics, 3rd ed., by JW Goodman. Englewood, CO: Roberts & Co. Publishers, 2005* **1** (2005).

[15] Tyson, R. K. and Frazier, B. W., [*Principles of adaptive optics*], CRC press (2022).